



1           **Rapid near-term warming in a carbon neutral future attributed**  
2                                   **to substantial aerosol decline**

3

4

5           Yang Yang<sup>1\*#</sup>, Li You<sup>1#</sup>, Hailong Wang<sup>2</sup>, Huimin Li<sup>1</sup>, Pinya Wang<sup>1</sup>, Hong Liao<sup>1</sup>

6

7

8           <sup>1</sup>Jiangsu Key Laboratory of Atmospheric Environment Monitoring and Pollution

9           Control, Joint International Research Laboratory of Climate and Environment Change

10           (ILCEC), Jiangsu Collaborative Innovation Center of Atmospheric Environment and

11           Equipment Technology, School of Environmental Science and Engineering, Nanjing

12           University of Information Science and Technology, Nanjing, Jiangsu, China

13           <sup>2</sup>Atmospheric, Climate, and Earth Sciences Division, Pacific Northwest National

14                                   Laboratory, Richland, Washington, USA

15

16

17

18           \*Correspondence to [yang.yang@nuist.edu.cn](mailto:yang.yang@nuist.edu.cn)

19           #These authors contributed equally: Yang Yang, Li You



20 **ABSTRACT**

21       Greenhouse gases (GHGs) and aerosols have been the main contributors to climate  
22 change. Here, future aerosols and GHGs impacts on global and regional surface air  
23 temperature (SAT) are assessed using machine learning. We show that, following a  
24 carbon-neutral pathway, global SAT rapidly increases by 0.8 °C from 2015 to 2050,  
25 with 0.6 °C attributed to the substantial decline in aerosols. Considering both the  
26 varying aerosols and GHGs, temperatures during 2015–2035 under the carbon-neutral  
27 scenario are even higher than those under the high-emission scenario, demonstrating  
28 that the near-term warming related to aerosol reduction is noteworthy, although carbon  
29 neutral scenario is beneficial to slow down the warming. If CO<sub>2</sub> is reduced to mitigate  
30 the warming caused by aerosol reduction, it has to decline from 400 ppm to 340–350  
31 ppm. This study emphasizes the importance of anthropogenic forcings in regulating  
32 climate change and reveals the dominant role of aerosols in modulating climate in the  
33 near-term carbon neutral future.

34



## 35 **1 Introduction**

36 According to the Intergovernmental Panel on Climate Change (IPCC) Sixth  
37 Assessment Report (AR6), the global-mean surface air temperature (GSAT) has  
38 increased by 1.09 °C in 2011–2020 relative to the average temperature of 1850–1900  
39 and is expected to rise by 1.5 °C or more over the next 20 years (IPCC, 2021). Some  
40 regions are experiencing more significant changes in mean surface air temperature  
41 (SAT) than the GSAT. For instance, since 1900, China's SAT has increased at a rate of  
42 1.3–1.7 °C per 100 years, which is significantly higher than the GSAT of 0.85 °C (Yan  
43 et al., 2020). The intensification of global warming has led to an increased variability  
44 in regional temperature, precipitation, and soil moisture (Sun et al., 2019; Ge et al.,  
45 2019; Du et al., 2022; Thackeray et al., 2022), which further worsened various types of  
46 extreme weather events and climate disasters in different regions of the globe (Guan et  
47 al., 2022; Tebaldi et al., 2021; Song et al., 2022). Therefore, understanding the  
48 underlying mechanisms of the temperature changes assists in better quantifying the  
49 contributions of anthropogenic and natural forcings to the observed increasing SAT and  
50 can improve observationally constrained projections of future climate change (Bône et  
51 al., 2022).

52 External forcings and internal variabilities have different effects on climate.  
53 External anthropogenic forcings include greenhouse gases (GHGs), anthropogenic  
54 aerosols, and land use (Ren et al., 2022; Wang et al., 2023; Yang et al., 2022, 2023).  
55 Volcanic emissions and solar radiation are examples of external natural forcing (Stenet  
56 and Kaufmann, 2014; Marotzke et al., 2015). Numerous studies have demonstrated that  
57 the rise in GHGs and changes in aerosols are the primary causes of the global warming  
58 observed during the 20th century (Folland et al., 2018; Jones et al., 2013). The increases  
59 in GHGs concentrations have led to a warming of 1.5 °C in 2010–2019 compared to  
60 1850–1900, with CO<sub>2</sub> and CH<sub>4</sub> contributions of 0.8 °C and 0.5 °C, respectively (Gillett  
61 et al., 2021; IPCC, 2021). Also, by analyzing the factors contributing to temperature  
62 changes, studies have shown that GHGs were the largest driver of global terrestrial  
63 warming in the period 1965–2014, leading to an increase of near-surface temperature  
64 by 0.3–2.0 °C in most land regions (Xu et al., 2024). The effect of aerosols on the  
65 radiation balance also led to changes in SAT (Gao et al., 2022, 2023; Liu et al., 2023),  
66 with black carbon (BC) being the second largest contributor to current global warming  
67 after CO<sub>2</sub> (Ramanathan and Carmichael, 2008; Yang et al., 2019; Xie et al., 2023).



68 Through interacting with radiation and clouds, aerosols have caused a cooling by 0.1–  
69 0.9 °C over most land regions during 1965–2014 (Xu et al., 2024), which partially offset  
70 global warming due to GHGs (Liu et al., 2019). Among aerosol species, anthropogenic  
71 sulfate has a cooling effect of 0.5 °C globally, almost offsetting the warming effect of  
72 CH<sub>4</sub> (IPCC, 2021). The rapid warming of the Arctic over the last three decades also had  
73 a contribution from the changes in anthropogenic sulfate and BC aerosols (Shindell and  
74 Faluvegi, 2009; Yang et al., 2018a; Ren et al., 2020). Additionally, natural forcings  
75 such as solar irradiance and volcanic forcing play a crucial role in temperature change  
76 (Folland et al., 2018). Land use/land cover change also directly contributes to  
77 temperature anomalies near the surface (Rigden et al., 2017; Li et al., 2015). Recent  
78 studies (e.g., Sweeney et al., 2023, 2024) found that climate system internal variabilities  
79 have contributed to the observed spatial pattern of Arctic warming and global cooling  
80 (mostly in the Tropical Eastern Pacific and Southern Ocean regions) in the last few  
81 decades (1980–2022). Using a pattern recognition algorithm based on machine learning  
82 (ML), they successfully partitioned the roles of internal variability and externally forced  
83 climate response.

84 ML has become a modern tool for regression tasks due to its computational  
85 efficiency and state-of-the-art performance (Li et al., 2022; Ni et al., 2024). Pasini et al.  
86 (2017) successfully reconstructed and attributed changes in GSAT from 1850 to 2010  
87 using an artificial neural network (ANN) combining forcings such as GHGs, BC,  
88 sulfate, solar activity, and volcanic forcing as input data. Their findings indicated that  
89 anthropogenic forcing played a dominant role in the recent global warming. Xiao et al.  
90 (2022) attributed GSAT changes to anthropogenic forcing, natural forcing, and internal  
91 variability for the period of 1866–2019 using a multilayer perceptron neural network  
92 technique and reported that anthropogenic forcing has increased the global surface  
93 temperature by approximately 1.2 °C from 1961 to 1990 and this technique presented  
94 outstanding reconstruction skills on variations in global surface temperature. These  
95 studies demonstrate that ML methods can effectively capture the nonlinear relationship  
96 between various forcings and temperatures, enabling the feasibility of studying  
97 temperature variations.

98 Emissions changes under various future scenarios are likely to lead to a diversity  
99 of climate changes. Therefore, predicting and attributing future changes in SAT can  
100 help understand climate change and shape mitigation strategies. In the latest Coupled  
101 Model Comparison Project Phase 6 (Eyring et al., 2016), the Detection and Attribution



102 Model Comparison Project (DAMIP) (Gillett et al., 2016) provides estimates of  
103 historically forced subsets (aerosols only, GHGs only, natural factors only) of  
104 temperature responses to assess the individual contribution of various external forcings  
105 to the observed global and regional climate change. Furthermore, simulations of  
106 aerosols, GHGs and natural forcings under future scenarios are also included in DAMIP.  
107 Nonetheless, the scenario simulations were conducted only under the medium Shared  
108 Socio-economic Pathway 2-4.5 (SSP2-4.5) scenario, which represents an intermediate  
109 level of future changes in GHGs, aerosols, and land use. The contributions of individual  
110 forcings to temperature under other emission scenarios are not yet available. To  
111 minimize the negative impacts and risks of climate change, several countries have  
112 committed to achieving carbon neutrality by the mid-21<sup>st</sup> century (De La Peña et al.,  
113 2022; Cheng et al., 2021). Ma et al. (2022) used the CESM1-CAM5 model to conduct  
114 aerosol radiative forcing simulations under the Representative Concentration Pathways  
115 2.6 (RCP2.6) scenarios that is near the low-warming target in future projections. They  
116 discovered that the cooling effect caused by the CO<sub>2</sub> decrease under the future low  
117 emission scenario would be overwhelmed by anomalous warming effects from  
118 reductions in anthropogenic aerosols for a relatively long time. In another study,  
119 CESM1 experiments were conducted to analyze temperature changes induced by GHGs,  
120 aerosols, and tropospheric ozone toward a carbon-neutral pathway (Wang et al., 2023).  
121 They showed that at the equilibrium status, warming across the globe induced by  
122 aerosol reductions would be more pronounced during the carbon-neutral period than  
123 changes in GHGs and tropospheric ozone. It suggests that aerosols dominate the change  
124 in future climate under a carbon-neutral pathway, challenging previous knowledge  
125 about the dominance of GHGs in climate change. However, the climate attributions  
126 under the carbon-neutral scenario in previous studies were based on single model  
127 simulations and the quantitative results are potentially model dependent.

128 Previous studies have shown that various factors can have distinct impacts on  
129 temperature changes under different future scenarios. Most studies only considered the  
130 SSP2-4.5 scenario based on CMIP6 DAMIP future simulations or results of individual  
131 climate models. In this study, ML methods are used to quantitatively analyze the  
132 contributions of GHGs and anthropogenic aerosols to future SAT changes in multiple  
133 SSP scenarios by combining CMIP6 multi-model temperature outputs, aerosol and  
134 precursor emissions, GHGs concentrations, and other auxiliary data (Fig. 1). The GSAT  
135 and regional mean SAT for 18 latitudinal bands from 90°S to 90°N, each spanning 10°,



136 are separately predicted. Three key regions including China, Europe and North America  
137 are also individually focused on to investigate the causes of temperature changes.  
138 Future scenarios, including the carbon neutral scenario (SSP1-1.9) and high emission  
139 scenario (SSP5-8.5), are analyzed to more accurately bound temperature changes in  
140 different regions, providing more precise climate change predictions and attribution  
141 analyses.

## 142 **2 Materials and methods**

### 143 **2.1 Surface air temperature data and driving forcings from CMIP6**

144 The CMIP6 multi-model simulations provide the global monthly mean SAT data.  
145 In this study, large SAT data from multiple CMIP6 experiments are used as the target  
146 variable to train ML models. The experiments include the historical simulations  
147 (hereafter referred to as historical), anthropogenic-aerosol-only historical simulations  
148 (hist-aer), well-mixed greenhouse-gas-only historical simulations (hist-GHG), natural-  
149 only historical simulations (hist-nat) and CO<sub>2</sub>-only historical simulations (hist-CO<sub>2</sub>)  
150 from DAMIP, the future-scenario climate simulations under SSP1-1.9, SSP1-2.6, SSP2-  
151 4.5, SSP3-7.0 and SSP5-8.5 scenarios (ssp119, ssp126, ssp245, ssp370 and ssp585,  
152 respectively) from the Scenario Model Comparison Program (ScenarioMIP) (O’Neill  
153 et al., 2016), and anthropogenic-aerosol-only future simulations (ssp245-aer) and well-  
154 mixed greenhouse-gas-only future simulations (ssp245-GHG) under SSP2-4.5 from  
155 DAMIP. The DAMIP simulations used here adopt the “single forcing” approach, in  
156 which simulations are driven by changes only in the individual forcing of interest,  
157 leaving other forcings at pre-industrial levels. The experiments are described and the  
158 models used are shown in Table S1.

159 Forcings affecting temperature are also collected from input4MIPs to train the  
160 ML models. Anthropogenic and biomass burning emissions of aerosols and  
161 precursors including BC, organic carbon, sulfur dioxide, GHGs concentrations, land  
162 use, solar radiation and volcanic forcings covering the historical period and various  
163 future pathways are selected as the input features for the ML models. See Table 1 for  
164 a description of the specific data.

### 165 **2.2 Machine learning methods**



166 Light Gradient Boosting Machine (LightGBM) and Extreme Gradient Boosting  
167 (XGBoost) are two of the most popular algorithms based on the Gradient Boosting ML  
168 technique, which have features of great explanatory power, high accuracy and  
169 efficiency (Friedman et al., 2001). XGBoost is an iterative decision tree algorithm  
170 (Friedman et al., 2001) that consists of multiple decision trees to make the final decision  
171 by iterating multiple trees together. Although XGBoost employs many engineering  
172 optimizations, it is still not as efficient and scalable as it should be with high feature  
173 dimensions and large amounts of data (Ke et al., 2017). LightGBM algorithm employs  
174 two new methods, Gradient-based One-Sided Sampling (GOSS) and Exclusive Feature  
175 Bundling (EFB) to ensure fast algorithm training and high accuracy. Compared with  
176 XGBoost, LightGBM has a faster training time, lower memory usage, more efficient  
177 processing of high-dimensional features, high parallelization capability, and lower  
178 hyperparameter tuning requirements (McCarty et al., 2020). In this study, the GSAT,  
179 zonal-mean SAT prediction models for individual latitudinal bands, and regional SAT  
180 prediction models for countries of China, Europe and North America are built mainly  
181 using LightGBM, while the XGBoost results are used for reference. The SAT prediction  
182 in this study also shows a higher accuracy and faster speed with LightGBM than  
183 XGBoost.

184 The following steps describe the specific procedure by which ML models attribute  
185 and predict SAT (Fig. 1) :

186 First, input data sets are created in the same way as the CMIP6 design for the ML  
187 model training. A large number of CMIP6 input variables for historical simulations,  
188 ScenarioMIP (ssp119, ssp126, ssp245, ssp370 and ssp585) and DAMIP (hist-aer, hist-  
189 GHG, hist-nat, hist-CO<sub>2</sub>, ssp245-aer and ssp245-GHG) are used to match the CMIP6  
190 SAT outputs. Multi-model mean SAT anomalies are calculated and employed as the  
191 target in the ML models.

192 Second, one ML model is trained for GSAT, eighteen models are trained for zonal  
193 SAT over latitudinal bands from 90°S to 90°N, each spanning 10°, and three models  
194 are trained for the three focused regions including China, Europe and North America.  
195 The input data sets are divided into two parts, with 90% for ML model training and 10%



196 for ML model testing. Note that the data for model training and testing are randomly  
197 selected since multiple CMIP6 simulations are involved and each of them has different  
198 time period and experimental design. The LightGBM hyperparameters, including  
199 `boosting_type` (type of algorithm), `objective` (optimized loss function), `num_leaves`  
200 (maximum number of leaf nodes in each tree), `num_boost_round` (total number of trees  
201 constructed), `learning_rate` (total number of trees constructed), `reg_alpha` (L1  
202 regularization), `reg_lambda` (L2 regularization), `colsample_bytree` (proportion of  
203 features used in training each tree), are tuned using the five-fold cross-validation for  
204 each ML model. The optimal hyperparameters (`boosting_type = gbdt`, `objective =`  
205 `regression`, `num_leave = 50`, `num_boost_round = 200`, `learning_rate = 0.1`, `reg_alpha =`  
206 `0.1`, `reg_lambda = 0.1`, `colsample_bytree = 0.9`) are utilized for the GSAT model. The  
207 coefficient of determination ( $R^2$ ), root mean square error (RMSE), and mean absolute  
208 error (MAE) are calculated to evaluate the performance of the ML models.

209 Third, future temperature changes induced by changes in anthropogenic aerosols  
210 and GHGs under various scenarios are predicted by using the trained ML models with  
211 varying emissions of aerosols and precursors and GHGs concentrations, respectively,  
212 for 2015–2100, while keeping other parameters at pre-industrial (1850) conditions.

### 213 **3 Results**

#### 214 **3.1 Predictive capability of machine learning models**

215 Figures 2, S1 and S2 show the density scatter plots of the predictive ability of the  
216 LightGBM models on the global, zonal, and regional SAT, respectively. The GSAT  
217 predicted by the model is in a good agreement with the CMIP6 results, with  $R^2$  reaching  
218 0.99, RMSE of 0.11 °C and MAE of 0.08 °C. The LightGBM can also well predict  
219 zonal and regional SAT with  $R^2$  mostly higher than 0.91, except over high latitudes of  
220 the Southern Hemisphere (70°–90°S), where  $R^2$  is in the range of 0.8–0.9. The metrics  
221 indicate that the model exhibits excellent performance and can accurately reconstruct  
222 global and regional temperature changes. Figure 2b illustrates the importance scores of  
223 the input features into the LightGBM model for predicting GSAT, a value that  
224 represents the proportion of each feature contributing to the model's prediction results.  
225 CO<sub>2</sub> is the most important parameter among all the input variables, with an importance  
226 of 14.4% to the model, which is consistent with previous studies that CO<sub>2</sub> contributed



227 the most to historical temperature variations (Stips et al., 2016; IPCC, 2021). CO<sub>2</sub> is  
228 also the most important feature influencing the models for zonal and regional SAT  
229 prediction (Figs. S2 and S3). In addition, CH<sub>4</sub> and anthropogenic emissions of black  
230 carbon (BC), organic carbon (OC) and sulfur dioxide (SO<sub>2</sub>) are also important factors  
231 in the global and regional temperature prediction models (Ramanathan and Carmichael,  
232 2008). The Shapley Additive Explanations (SHAP) values, which explain the extent  
233 and direction of the influence of each feature to the model's outcome, are also shown  
234 in Fig. S4. From the SHAP calculation, GHGs, such as CO<sub>2</sub> and N<sub>2</sub>O, contribute  
235 positively to the temperature change globally and regionally. Anthropogenic emissions  
236 of SO<sub>2</sub> also largely contribute to the temperature change, leading to the decreases in  
237 global and regional SAT. However, due to the dominant role of sulfate among all  
238 aerosols in historical climate change and the CMIP6 data do not have the individual  
239 attribution simulations for scattering and absorbing aerosols as the input for ML models,  
240 BC does not present a warming effect as expected in the ML models. It suggests that  
241 more attribution simulations are required in the future CMIP protocols.

242 Figure 3 depicts the LightGBM-predicted and the corresponding CMIP6 historical  
243 and future temperature anomalies over 1850–2100 under SSP1-1.9 and SSP5-8.5  
244 scenarios relative to the 1850 level. The LightGBM-predicted temperatures are in  
245 nearly perfect agreement with the CMIP6 simulations and can reliably forecast  
246 historical and future temperature trends. Figure 3d displays the historical temperature  
247 anomalies attributed to the changes in GHGs, CO<sub>2</sub>, anthropogenic aerosols and natural  
248 forcings projected by the CMIP6 and LightGBM models. Anthropogenic emissions of  
249 aerosols acted as cooling agents from 1850 to 2020, and the aerosol cooling trend was  
250 stabilized around 1990, related to the aerosol decline in Europe and North America  
251 (Yang et al., 2018, 2020). The GHGs and CO<sub>2</sub> alone have consistently led to significant  
252 warming across the globe, while natural factors such as solar radiation and volcanic  
253 activity contributed to the interannual variability but minimally to temperature trends.  
254 It indicates that the LightGBM model can accurately attribute the contribution of  
255 various factors to historical temperature variations.

### 256 **3.2 Attribution of global surface air temperature changes under future scenarios**



257 To improve the assessments of future climate change, the attributions are carried  
258 out based on ML methods under future scenarios. First of all, it is crucial to evaluate  
259 the accuracy of the ML model for future temperature attribution. Figure 4 shows the  
260 LightGBM-predicted GSAT anomalies over 2021–2100 relative to 1850 attributed to  
261 total forcings, anthropogenic aerosols, and GHGs under the SSP2-4.5 scenario. With  
262 all forcings, the LightGBM can perfectly reproduce the temperature variations, with  
263 GSAT anomaly increasing from 1.3 °C in 2021 to 2.6 °C in 2050 and 4.0 °C in 2100.  
264 The future warming under the intermediate forcing scenario is primarily due to the  
265 increase in GHGs predicted by both CMIP6 and LightGBM, while the decline of  
266 anthropogenic aerosols also contributes to the warming. The LightGBM can also  
267 perfectly predict changes in regional SAT in 2095 relative to 2020 attributed to  
268 anthropogenic aerosols and GHGs under the SSP2-4.5 scenario over China, Europe,  
269 and North America compared to the CMIP6 predictions (Figs. S5-S7). Therefore, it is  
270 feasible to attribute future SAT changes to GHGs and anthropogenic aerosols with ML  
271 methods.

272 Using the trained LightGBM model along with GHGs concentrations,  
273 anthropogenic emissions of aerosols and precursors, attributions of SAT anomalies to  
274 future changes in anthropogenic aerosols and GHGs under the carbon neutral (SSP1-  
275 1.9) and high emission (SSP5-8.5) scenarios are estimated. Following the carbon  
276 neutral pathway, GSAT rapidly increases by 0.8 °C from 2015 to 2050, then slightly  
277 decreases until 2100 (Fig. 3b). As shown in Fig. 5a, the rapid warming is dominated by  
278 the changes in anthropogenic aerosols, resulting from the rapid decline in future  
279 anthropogenic emissions of aerosols and precursors (Fig. S8). It contributes to warming  
280 by 0.6 °C, while the rest 0.2 °C is attributed to the changes in GHGs. It suggests that  
281 aerosol changes will overtake GHGs in causing a warmer climate toward carbon  
282 neutrality. In the second half of the 21<sup>st</sup> century, the cooling effect of anthropogenic  
283 aerosols is significantly weakened and the decreases in GHGs contribute to the cooling  
284 of the Earth. Under the high emission scenario, GSAT shows a monotonic increase by  
285 more than 5 °C during 2015–2100 (Fig. 3c). Majority of the warming is from the  
286 substantial increases in GHGs, while aerosols exert a minor role in the warming trend  
287 (Fig. 5b).

288 Figures 5c and 5d show the difference in GSAT between the carbon neutral and  
289 high emission scenarios due to the future changes in anthropogenic aerosols, GHGs and  
290 both of them. Compared to the high emission scenario, the rapid decline of



291 anthropogenic aerosols causes a fast warming by 0.55 °C across the globe between 2015  
292 and 2035 in the carbon neutral scenario and this warming is then dampened to 0.35 °C  
293 at the end of the 21<sup>st</sup> century associated with the follow-up aerosol reductions in the  
294 high emission scenario. Due to the carbon control measures, lower GHGs levels in the  
295 carbon neutral compared to high emission scenario result in a strong cooling effect by  
296 4 °C during 2015–2100. It is interesting that unlike the common wisdom that the carbon  
297 neutral would cool the Earth relative to the high emission scenario, the GSAT increases  
298 during 2015–2035 (Fig. 5d), attributed to the rapid decline in anthropogenic aerosols.  
299 It demonstrates that although the carbon neutral scenario is beneficial in slowing down  
300 the temperature rise, the near-term warming related to aerosol reduction is noteworthy.

### 301 **3.3 Attribution of latitudinal and regional temperature changes**

302 To investigate the causes of global near-term (2021–2030), medium-term (2045–  
303 2054) and long-term (2091–2100) future temperature changes, SAT changes in each  
304 10° latitudinal band from 90°S to 90°N are predicted in 18 LightGBM models and the  
305 attributions to anthropogenic aerosols and GHGs are analyzed here under the SSP1-1.9  
306 and SSP5-8.5 scenarios. Following the carbon neutral pathway, substantial reductions  
307 in anthropogenic aerosols cause warming over most latitudinal bands of the globe and  
308 the warming is generally stronger than in the high emission scenario over the polluted  
309 mid- and high latitudes of the Northern Hemisphere, relative to 2020 (Figs. 6a, 6d and  
310 6g). As the in-depth aerosol reduction from the short-term to long-term future, the  
311 warming is intensified toward carbon neutrality. The GHGs show diverse contributions  
312 under the carbon neutral and high emissions scenarios compared to the aerosol  
313 contributions. Under the high emission scenario, continuous rises in GHGs induce a  
314 sustained climate warming throughout the 21<sup>st</sup> century (Figs. 6b, 6e and 6h), with the  
315 SAT increase by 2–4 °C in low and mid-latitudes and 4–9 °C in high-latitude regions  
316 in the long-term future compared to 2020. For the carbon neutral scenario, the zero-  
317 carbon policies contribute to weaker warming in the near-term future compared to the  
318 high emission scenario and even a slight cooling over most latitude bands in the long-  
319 term future relative to 2020. It suggests that toward carbon neutrality, changes in  
320 anthropogenic aerosols dominate the future climate, while the changes in GHGs control  
321 the climate under the high emission scenario. The combined effect of GHGs and  
322 anthropogenic aerosols results in a warmer climate in the future under both carbon  
323 neutral and high emission scenarios (Figs. 6c, 6f and 6i).



324           However, beyond the expectation that the carbon neutral would cool the Earth, in  
325 the near-term future, the warming induced by the combined effect of aerosols and  
326 GHGs under the carbon neutral scenario is surprisingly stronger than that under the  
327 high emission scenario over most mid-latitude regions (Fig. 6c). This anomalous  
328 warming is attributed to the substantial aerosol decline in the near-term future,  
329 especially over the polluted mid-latitude regions. The warming in the high latitudes is  
330 stronger in high emission scenario than carbon neutral scenario controlled by the  
331 increases in GHGs, because GHGs are more uniformly distributed in the atmosphere  
332 together with the Arctic amplification. As the slowdown of emission reductions in  
333 aerosols and precursors in the medium-term future (Fig. S8), the combined warming  
334 under the high emission scenario surpasses that under the carbon neutral scenario (Fig.  
335 6f) and the SAT is warmer by 3–10 °C under the high emission scenario than the carbon  
336 neutral scenario in the long-term future (Fig. 6i). These again suggest that although the  
337 carbon neutral pathway alleviates the temperature rise, the anomalous warming mainly  
338 caused by the rapid aerosol decline over the polluted mid-latitude regions in the near-  
339 term future should be considered in the climate mitigation.

340           The regional changes in SAT over China, Europe and North America due to future  
341 changes in anthropogenic aerosols and GHGs in 2095 relative to 2020 under the SSP1-  
342 1.9 and SSP5-8.5 scenarios are shown in Figures 7-9, respectively. Predicted by the  
343 LightGBM model, by the end of the 21<sup>st</sup> century, reductions in anthropogenic aerosols  
344 lead to a dramatic regional warming by 0.75 °C, 0.68 °C and 0.67 °C over China,  
345 Europe and North America, respectively, following the carbon-neutral pathway, while  
346 the SAT changes due to GHGs are weak and insignificant (–0.2 °C, 0.00 °C and –  
347 0.15 °C). In the high emission scenario, on the contrary, the warming caused by rising  
348 GHGs in China, Europe and North America is significantly higher than that caused by  
349 anthropogenic aerosols, causing regional warming by 5.02 °C, 4.61 °C and 5.28 °C in  
350 China, Europe, and North America, respectively, in 2095 relative to 2020.

### 351 **3.4 Implications of future temperature attribution with machine learning**

352           The ML can provide an efficient way for predicting future changes in temperature,  
353 which also provide guidance for designing future emission pathways. Here we show  
354 one example of using the temperature attribution model. Based on the analysis above,  
355 we found that reductions in anthropogenic aerosols have a much stronger warming  
356 effect on GSAT than GHGs in the SSP1-1.9 scenario. CO<sub>2</sub> is the primary contributor



357 among all GHGs to the historical variation in temperature. One possible method for  
358 mitigating aerosol-induced warming under the SSP1-1.9 scenario is to reduce CO<sub>2</sub>  
359 further.

360 As shown in Fig. 10a, based on the LightGBM model for the GSAT prediction  
361 driven by the changes in CO<sub>2</sub> alone, future GSAT is projected to increase by about  
362 0.3 °C during 2015–2040, then decrease to the 2020 level at the end of the 21<sup>st</sup> century  
363 due to the changes in CO<sub>2</sub> under the SSP1-1.9 scenario. The temperature change is in  
364 accordance with the change in global mean CO<sub>2</sub> concentration, increasing from 400  
365 ppm in 2015 to 440 ppm in 2040 and decreasing after 2040 (Fig. 10b). If we were to  
366 reduce the CO<sub>2</sub> for mitigating the aerosol reduction-induced warming shown in Fig. 5a,  
367 the CO<sub>2</sub>-induced GSAT should be continuously decreased by 0.7 °C during 2015–2100,  
368 which translates to a CO<sub>2</sub> concentration decline from 400 ppm to 340–350 ppm. It  
369 provides a more intuitive experience of the significant warming caused by aerosol  
370 decline in terms of CO<sub>2</sub> changes but does not mean CO<sub>2</sub> concentrations should be  
371 reduced to this low level.

#### 372 **4 Conclusion and discussions**

373 Future emissions changes under various scenarios can lead to diverse changes in  
374 climate and understanding the factors underlying the climate changes assists in better  
375 designing future pathways. ML technique enables more efficient and effective  
376 attribution of temperature change than traditional global climate models. In this study,  
377 ML models are trained using forcing factors such as anthropogenic and biomass burning  
378 emissions of aerosols and precursors, GHGs, land use, solar radiation, and volcanoes  
379 to predict the SAT for the globe, individual latitude zones, and three key regions  
380 (including China, Europe, and North America) under the SSP1-1.9 and SSP5-5.8  
381 scenarios for 2015–2100, which are used to analyze the impacts of anthropogenic  
382 aerosols and GHGs on future temperature changes. The GSAT predicted by the  
383 LightGBM model is in a good agreement with the CMIP6 results, with R<sup>2</sup> reaching 0.99,  
384 RMSE of 0.11 °C and MAE of 0.08 °C.

385 Based on the ML method, we show that following the carbon neutral pathway  
386 GSAT rapidly increases by 0.8 °C from 2015 to 2050, then slightly decreases until 2100.  
387 The substantial decline in anthropogenic aerosols dominates the warming, contributing  
388 0.6 °C of the SAT increase, while the rest 0.2 °C is attributed to the future changes in  
389 GHGs. However, GHGs dominate GSAT changes in the high forcing scenario,



390 contributing 5 °C of warming during 2015–2100. More importantly, compared to the  
391 high emission scenario, the GSAT increases under the carbon neutral scenario during  
392 2015–2035, which is attributed to the rapid decline in anthropogenic aerosols,  
393 demonstrating that the near-term warming related to aerosol reduction is noteworthy,  
394 although the carbon neutral scenario slows down the temperature rise in the long run.  
395 The warming induced by aerosol reductions is strong over the polluted mid- and high  
396 latitudes of the Northern Hemisphere, causing a SAT increase by 0.75 °C, 0.68 °C and  
397 0.67 °C over China, Europe and North America, respectively, in 2095 relative to 2020  
398 under the carbon-neutral pathway. Under the high emission scenario, the continued rise  
399 in future GHGs leads to a much warmer climate than in 2020, leading to a regional  
400 warming of 5.02 °C, 4.61 °C and 5.28 °C in China, Europe and North America,  
401 respectively, in 2095 relative to 2020. The results highlight the importance of changes  
402 in anthropogenic forcings in regulating future climate change and reveal a dominant  
403 role of aerosols in modulating climate in the near-term carbon neutral future. In addition,  
404 our study suggests that if CO<sub>2</sub> is reduced to mitigate the warming caused by reduced  
405 aerosols in the SSP1-1.9 scenario, CO<sub>2</sub>-induced GSAT needs to decline by 0.7 °C over  
406 the period 2015–2100, which translates to a decline of CO<sub>2</sub> concentration from 400  
407 ppm to 340–350 ppm.

408 To reduce the ML model dependence, we also analyzed global, latitudinal band  
409 and regional temperature prediction and attribution using the XGBoost model. The  
410 GSAT predicted by XGBoost is in a good agreement with the LightGBM model, with  
411 the R<sup>2</sup> reaching 0.99 (Fig. S9). However, LightGBM shows a higher R<sup>2</sup>, lower RMSE  
412 and MAE for regional SAT prediction than XGBoost. Therefore, the LightGBM model  
413 is better utilized for temperature attribution analysis in this study. Also, comparing the  
414 results of temperature attribution for global mean, latitudinal band, and regional mean  
415 under the SSP1-1.9 and SSP5-8.5 scenarios predicted by the LightGBM and XGBoost  
416 models, the results are similar between the two ML models (Figs. S10-14).

417 It should be noted that there are some uncertainties in ML prediction and  
418 attribution of future SAT changes. The effect of aerosols on climate is complex, as they  
419 can affect the Earth's energy balance directly by scattering and absorbing radiation (Yu  
420 et al., 2006) and indirectly by interacting with clouds (Lohmann et al., 2005). Thus, the  
421 complexity of such interactions mechanisms makes the spatial pattern of aerosol  
422 impacts on climate more difficult to be captured and predicted by ML models. In  
423 particular, changes in anthropogenic aerosols can lead to temperature changes in remote



424 regions through slow feedbacks from the oceans (Gao et al., 2023). At the same time,  
425 transboundary long-range transport of aerosols (Huang et al., 2020; Jaffe et al., 1999)  
426 can also influence local climate, which cannot be considered in the ML models directly  
427 using local emissions as the aerosol predictor.

428 In future researches, ML can be equipped with the physical, chemical and  
429 dynamical processes of aerosols and their interactions with radiation and clouds derived  
430 from both models and observations to better capture the complex roles of aerosols in  
431 the climate system and thus provide more realistic predictions of aerosol climate effects.  
432 Moreover, this study mainly focuses on anthropogenic aerosols. Natural aerosols from  
433 biomass burning, biogenic emissions, marine and desert are also sensitive to climate  
434 change and can feedback on future climate, which are also encouraged to be embodied  
435 in the ML. Additionally, different aerosol species exert different impacts on climate.  
436 For example, BC generally produces a warming effect on climate system, whereas SO<sub>2</sub>  
437 leads to a cooling. However, current ML is hard to learn the individual effects of such  
438 signature because CMIP6 only provides attribution experiments for the entire  
439 anthropogenic aerosol variation, which limits our ability to more accurately quantify  
440 the impacts of different pollutants. More simulation experiments about the effects of  
441 individual pollutants are suggested to be considered in the future multi-model  
442 comparison protocols.

443 We also note that using different machine learning algorithms may affect the  
444 results. Neural networks have been widely used in climate researches because they are  
445 able to represent complex nonlinear relationships between input and output variables  
446 and have the ability to self-learn from data. In this study, LightGBM algorithm is  
447 applied, mainly due to the fact that LightGBM is more efficient in terms of training  
448 speed and memory usage when dealing with large datasets, which is particularly  
449 suitable for the huge climate datasets from CMIP6 multiple scenarios in this study.  
450 Additionally, LightGBM provides better model interpretability through metrics such as  
451 feature importances and SHAP values, which is crucial in climate attribution studies.



452 **Code and data availability**

453 Global near-surface mean temperature data are available from the Sixth International  
454 Coupled Model Comparison Program (CMIP6) ([https://esgf-  
455 node.llnl.gov/search/cmip6/](https://esgf-node.llnl.gov/search/cmip6/)). Anthropogenic and biomass burning emissions of  
456 aerosols and precursors, greenhouse gases, land use, solar radiation, and volcanic  
457 forcing can be downloaded from input4MIPs ([https://esgf-  
458 node.llnl.gov/search/input4mips/](https://esgf-node.llnl.gov/search/input4mips/)). The data and code are available at  
459 <https://doi.org/10.5281/zenodo.14166811>.

460

461 **Author contributions**

462 YY designed the research. LY performed the model simulations, analyzed data and  
463 wrote the initial draft. All the authors discussed the results and contributed to the final  
464 manuscript.

465

466 **Competing Interest**

467 At least one of the (co-)authors is a member of the editorial board of ACP.

468

469 **Acknowledgments**

470 The Pacific Northwest National Laboratory (PNNL) is operated for DOE by the Battelle  
471 Memorial Institute under contract DE-AC05-76RLO1830.

472

473 **Financial support**

474 This study was supported by the National Natural Science Foundation of China (grant  
475 42475032), Jiangsu Science Fund for Carbon Neutrality (grant BK20220031) and  
476 Jiangsu Innovation Research Group (grant JSSCTD202346).

477



478 **Reference**

- 479 Bône, C., Gastineau, G., Thiria, S., and Gallinari, P.: Detection and attribution of  
480 climate change: A deep learning and variational approach, *Environ. Data Sci.*, 1,  
481 e27, <https://doi.org/10.1017/eds.2022.17>, 2022.
- 482 Cheng, J., Tong, D., Zhang, Q., Liu, Y., Lei, Y., Yan, G., Yan, L., Yu, S., Cui, R. Y.,  
483 Clarke, L., Geng, G., Zheng, B., Zhang, X., Davis, S. J., and He, K.: Pathways of  
484 China's PM<sub>2.5</sub> air quality 2015–2060 in the context of carbon neutrality, *Natl. Sci.*  
485 *Rev.*, 8, nwab078, <https://doi.org/10.1093/nsr/nwab078>, 2021.
- 486 De La Peña, L., Guo, R., Cao, X., Ni, X., and Zhang, W.: Accelerating the energy  
487 transition to achieve carbon neutrality, *Resour. Conserv. Recycl.*, 177, 105957,  
488 <https://doi.org/10.1016/j.resconrec.2021.105957>, 2022.
- 489 Du, H., Donat, M. G., Zong, S., Alexander, L. V., Manzanar, R., Kruger, A., Choi, G.,  
490 Salinger, J., He, H. S., Li, M.-H., Fujibe, F., Nandintsetseg, B., Rehman, S., Abbas,  
491 F., Rusticucci, M., Srivastava, A., Zhai, P., Lippmann, T., Yabi, I., Stambaugh, M.  
492 C., Wang, S., Batbold, A., Oliveira, P. T. de, Adrees, M., Hou, W., Silva, C. M. S.  
493 e, Lucio, P. S., and Wu, Z.: Extreme Precipitation on Consecutive Days Occurs  
494 More Often in a Warming Climate, *Bull. Am. Meteorol. Soc.*, 103, 1130–1145,  
495 <https://doi.org/10.1175/BAMS-D-21-0140.1>, 2022.
- 496 Eyring, V., Bony, S., Meehl, G. A., Senior, C. A., Stevens, B., Stouffer, R. J., and Taylor,  
497 K. E.: Overview of the Coupled Model Intercomparison Project Phase 6 (CMIP6)  
498 experimental design and organization, *Geosci. Model Dev.*, 9, 1937–1958,  
499 <https://doi.org/10.5194/gmd-9-1937-2016>, 2016.
- 500 Folland, C. K., Boucher, O., Colman, A., and Parker, D. E.: Causes of irregularities in  
501 trends of global mean surface temperature since the late 19th century, *Sci. Adv.*, 4,  
502 eaao5297, <https://doi.org/10.1126/sciadv.aao5297>, 2018.
- 503 Friedman, J. H.: Greedy function approximation: A gradient boosting machine, *Ann.*  
504 *Stat.*, 29, <https://doi.org/10.1214/aos/1013203451>, 2001.
- 505 Gao, J., Yang, Y., Wang, H., Wang, P., Li, H., Li, M., Ren, L., Yue, X., and Liao, H.:



- 506 Fast climate responses to emission reductions in aerosol and ozone precursors in  
507 China during 2013–2017, *Atmos. Chem. Phys.*, 22, 7131–7142,  
508 <https://doi.org/10.5194/acp-22-7131-2022>, 2022.
- 509 Gao, J., Yang, Y., Wang, H., Wang, P., Li, B., Li, J., Wei, J., Gao, M., and Liao, H.:  
510 Climate responses in China to domestic and foreign aerosol changes due to clean  
511 air actions during 2013–2019, *Npj Clim. Atmos. Sci.*, 6, 160,  
512 <https://doi.org/10.1038/s41612-023-00488-y>, 2023.
- 513 Ge, F., Zhu, S., Peng, T., Zhao, Y., Sielmann, F., Fraedrich, K., Zhi, X., Liu, X., Tang,  
514 W., and Ji, L.: Risks of precipitation extremes over Southeast Asia: does 1.5 °C or  
515 2 °C global warming make a difference? *Environ. Res. Lett.*, 14, 044015,  
516 <https://doi.org/10.1088/1748-9326/aaff7e>, 2019.
- 517 Gillett, N. P., Shiogama, H., Funke, B., Hegerl, G., Knutti, R., Matthes, K., Santer, B.  
518 D., Stone, D., and Tebaldi, C.: The Detection and Attribution Model  
519 Intercomparison Project (DAMIP v1.0) contribution to CMIP6, *Geosci. Model*  
520 *Dev.*, 9, 3685–3697, <https://doi.org/10.5194/gmd-9-3685-2016>, 2016.
- 521 Gillett, N. P., Kirchmeier-Young, M., Ribes, A., Shiogama, H., Hegerl, G. C., Knutti,  
522 R., Gastineau, G., John, J. G., Li, L., Nazarenko, L., Rosenbloom, N., Seland, Ø.,  
523 Wu, T., Yukimoto, S., and Ziehn, T.: Constraining human contributions to observed  
524 warming since the pre-industrial period, *Nat. Clim. Change*, 11, 207–212,  
525 <https://doi.org/10.1038/s41558-020-00965-9>, 2021.
- 526 Guan, X., Gao, Z., Huang, J., Cao, C., Zhu, K., and Wang, J.: Speeding extreme cold  
527 events under global warming, *Environ. Res. Lett.*, 17, 084012,  
528 <https://doi.org/10.1088/1748-9326/ac8110>, 2022.
- 529 Huang, X., Ding, A., Wang, Z., Ding, K., Gao, J., Chai, F., and Fu, C.: Amplified  
530 transboundary transport of haze by aerosol–boundary layer interaction in China,  
531 *Nat. Geosci.*, 13, 428–434, <https://doi.org/10.1038/s41561-020-0583-4>, 2020.
- 532 IPCC: Climate change 2021: The physical science basis. Contribution of Working  
533 Group I to the sixth assessment report of the intergovernmental panel on climate



- 534 change, Cambridge, UK, Cambridge University Press,  
535 <https://doi.org/10.1017/9781009157896>, 2021.
- 536 Jaffe, D., Anderson, T., Covert, D., Kotchenruther, R., Trost, B., Danielson, J., Simpson,  
537 W., Berntsen, T., Karlsdottir, S., Blake, D., Harris, J., Carmichael, G., and Uno, I.:  
538 Transport of Asian air pollution to North America, *Geophys. Res. Lett.*, 26, 711–  
539 714, <https://doi.org/10.1029/1999GL900100>, 1999.
- 540 Jones, G. S., Stott, P. A., and Christidis, N.: Attribution of observed historical near-  
541 surface temperature variations to anthropogenic and natural causes using CMIP5  
542 simulations, *J. Geophys. Res. Atmos.*, 118, 4001–4024,  
543 <https://doi.org/10.1002/jgrd.50239>, 2013.
- 544 Ke, G., Meng, Q., Finley, T., Wang, T., Chen, W., Ma, W., Ye Q., and Liu T.-Y.:  
545 LightGBM: a highly efficient gradient boosting decision tree. In *Proc. NeurIPS*,  
546 3146–3154, 2017.
- 547 Li, H., Yang, Y., Wang, H., Wang, P., Yue, X., and Liao, H.: Projected Aerosol Changes  
548 Driven by Emissions and Climate Change Using a Machine Learning Method,  
549 *Environ. Sci. Technol.*, 56, 3884–3893, <https://doi.org/10.1021/acs.est.1c04380>,  
550 2022.
- 551 Li, Y., Zhao, M., Motesharrei, S., Mu, Q., Kalnay, E., and Li, S.: Local cooling and  
552 warming effects of forests based on satellite observations, *Nat. Commun.*, 6, 6603,  
553 <https://doi.org/10.1038/ncomms7603>, 2015.
- 554 Liu, C., Yang, Y., Wang, H., Ren, L., Wei, J., Wang, P., and Liao, H.: Influence of Spatial  
555 Dipole Pattern in Asian Aerosol Changes on East Asian Summer Monsoon, *J.*  
556 *Climate*, 36, 1575–1585, <https://doi.org/10.1175/JCLI-D-22-0335.1>, 2023.
- 557 Liu, S., Xing, J., Zhao, B., Wang, J., Wang, S., Zhang, X., and Ding, A.: Understanding  
558 of Aerosol–Climate Interactions in China: Aerosol Impacts on Solar Radiation,  
559 Temperature, Cloud, and Precipitation and Its Changes Under Future Climate and  
560 Emission Scenarios, *Curr. Pollut. Rep.*, 5, 36–51, [https://doi.org/10.1007/s40726-](https://doi.org/10.1007/s40726-019-00107-6)  
561 019-00107-6, 2019.



- 562 Lohmann, U. and Feichter, J.: Global indirect aerosol effects: a review, *Atmos. Chem.*  
563 *Phys.*, 5, 715–737, <https://doi.org/10.5194/acp-5-715-2005>, 2005.
- 564 Ma, J., Cheng, J. C., Xu, Z., Chen, K., Lin, C., and Jiang, F.: Identification of the most  
565 influential areas for air pollution control using XGBoost and Grid Importance  
566 Rank, *J. Clean. Prod.*, 274, 122835, <https://doi.org/10.1016/j.jclepro.2020.122835>,  
567 2020.
- 568 Marotzke, J., Forster, P. M.: Forcing, feedback and internal variability in global  
569 temperature trends, *Nature*, 517, 565–570, <https://doi.org/10.1038/nature14117>,  
570 2015.
- 571 McCarty, D. A., Kim, H. W., and Lee, H. K.: Evaluation of light gradient boosted  
572 machine learning technique in large scale land use and land cover classification.  
573 *Environments*, 7(10), 84, <https://doi.org/10.3390/environments7100084>, 2020.
- 574 Ni, Y., Yang, Y., Wang, H., Li, H., Li, M., Wang, P., Li, K., and Liao, H.: Contrasting  
575 changes in ozone during 2019–2021 between eastern and the other regions of  
576 China attributed to anthropogenic emissions and meteorological conditions, *Sci.*  
577 *Total Environ.*, 908, 168272, <https://doi.org/10.1016/j.scitotenv.2023.168272>,  
578 2024.
- 579 O’Neill, B. C., Tebaldi, C., Van Vuuren, D. P., Eyring, V., Friedlingstein, P., Hurtt, G.,  
580 Knutti, R., Kriegler, E., Lamarque, J.-F., Lowe, J., Meehl, G. A., Moss, R., Riahi,  
581 K., and Sanderson, B. M.: The Scenario Model Intercomparison Project  
582 (ScenarioMIP) for CMIP6, *Geosci. Model Dev.*, 9, 3461 – 3482,  
583 <https://doi.org/10.5194/gmd-9-3461-2016>, 2016.
- 584 Pasini, A., Racca, P., Amendola, S., Cartocci, G., and Cassardo, C.: Attribution of recent  
585 temperature behaviour reassessed by a neural-network method, *Sci. Rep.*, 7, 17681,  
586 <https://doi.org/10.1038/s41598-017-18011-8>, 2017.
- 587 Ramanathan, V., and Carmichael, G.: Global and regional climate changes due to black  
588 carbon, *Nat. Geosci.*, 1, 221–227, <https://doi.org/10.1038/ngeo156>, 2008.
- 589 Ren, L., Yang, Y., Wang, H., Zhang, R., Wang, P., and Liao, H.: Source attribution of  
590 Arctic black carbon and sulfate aerosols and associated Arctic surface warming



- 591 during 1980–2018, *Atmos. Chem. Phys.*, 20, 9067–9085,  
592 <https://doi.org/10.5194/acp-20-9067-2020>, 2020.
- 593 Ren, L., Yang, Y., Wang, H., Wang, P., Yue, X., and Liao, H.: Widespread wildfires over  
594 the western United States in 2020 linked to emissions reductions during COVID-  
595 19, *Geophys. Res. Lett.*, 49, e2022GL099308, <https://doi.org/10.1029/2022GL099308>, 2022.
- 596
- 597 Rigden, A. J. and Li, D.: Attribution of surface temperature anomalies induced by land  
598 use and land cover changes, *Geophys. Res. Lett.*, 44, 6814–6822,  
599 <https://doi.org/10.1002/2017GL073811>, 2017.
- 600 Shindell, D., and Faluvegi, G.: Climate response to regional radiative forcing during  
601 the twentieth century, *Nat. Geosci.*, 2, 294–300,  
602 <https://doi.org/10.1038/NGEO473>, 2009.
- 603 Song, F., Zhang, G. J., Ramanathan, V., and Leung, L. R.: Trends in surface equivalent  
604 potential temperature: A more comprehensive metric for global warming and  
605 weather extremes, *Proc. Natl. Acad. Sci.*, 119, e2117832119,  
606 <https://doi.org/10.1073/pnas.2117832119>, 2022.
- 607 Stern, D. I., and Kaufmann, R. K.: Anthropogenic and natural causes of climate change,  
608 *Clim. Change*, 122, 257–269, <https://doi.org/10.1007/s10584-013-1007-x>, 2014.
- 609 Stips, A., Macias, D., Coughlan, C., Garcia-Gorriz, E., and Liang, X. S.: On the causal  
610 structure between CO<sub>2</sub> and global temperature, *Sci. Rep.*, 6, 21691,  
611 <https://doi.org/10.1038/srep21691>, 2016.
- 612 Sun, C., Jiang, Z., Li, W., Hou, Q., and Li, L.: Changes in extreme temperature over  
613 China when global warming stabilized at 1.5 °C and 2.0 °C, *Sci. Rep.*, 9, 14982,  
614 <https://doi.org/10.1038/s41598-019-50036-z>, 2019.
- 615 Sweeney, A. J., Fu, Q., Po-Chedley, S., Wang, H., and Wang, M.: Internal variability  
616 increased Arctic amplification during 1980 – 2022. *Geophys. Res. Lett.*, 50,  
617 e2023GL106060, <https://doi.org/10.1029/2023GL106060>, 2023.
- 618 Sweeney, A. J., Fu, Q., Po-Chedley, S., Wang, H., and Wang, M.: Unique temperature



- 619 trend pattern associated with internally driven global cooling and Arctic warming  
620 during 1980 – 2022. *Geophys. Res. Lett.*, 51, e2024GL108798,  
621 <https://doi.org/10.1029/2024GL108798>, 2024.
- 622 Tebaldi, C., Ranasinghe, R., Vousdoukas, M., Rasmussen, D. J., Vega-Westhoff, B.,  
623 Kirezci, E., Kopp, R. E., Sriver, R., and Mentaschi, L.: Extreme sea levels at  
624 different global warming levels, *Nat. Clim. Change*, 11, 746–751,  
625 <https://doi.org/10.1038/s41558-021-01127-1>, 2021.
- 626 Thackeray, C. W., Hall, A., Norris, J., and Chen, D.: Constraining the increased  
627 frequency of global precipitation extremes under warming, *Nat. Clim. Change*, 12,  
628 441–448, <https://doi.org/10.1038/s41558-022-01329-1>, 2022.
- 629 Wang, P., Yang, Y., Xue, D., Ren, L., Tang, J., Leung, L. R., and Liao, H.: Aerosols  
630 overtake greenhouse gases causing a warmer climate and more weather extremes  
631 toward carbon neutrality, *Nat. Commun.*, 14, 7257,  
632 <https://doi.org/10.1038/s41467-023-42891-2>, 2023.
- 633 Xiao, H.-X., Liu, X., Yu, R., Yao, B., Zhang, F., and Wang, Y.-Q.: Contributions of  
634 internal climate variability in driving global and ocean temperature variations  
635 using multi-layer perceptron neural network, *Adv. Clim. Change Res.*, 13, 459–  
636 472, <https://doi.org/10.1016/j.accre.2022.06.001>, 2022.
- 637 Xie, B., Yang, Y., Wang, H., Wang, P., and Liao, H.: Biomass Burning Emissions of  
638 Black Carbon over the Maritime Continent and ENSO Variability, *J. Climate*, 36,  
639 8365–8376, <https://doi.org/10.1175/JCLI-D-22-0553.1>, 2023.
- 640 Xu, C., Zhao, T., Zhang, J., Hua, L., and Tao, L.: Impacts of natural and anthropogenic  
641 forcings on historical and future changes in global-land surface air temperature in  
642 CMIP6–DAMIP simulations, *Climatic Change*, 177, 30,  
643 <https://doi.org/10.1007/s10584-024-03686-6>, 2024.
- 644 Yan, Z., Ding, Y., Zhai, P., Song, L., Cao, L., and Li, Z.: Re-Assessing Climatic  
645 Warming in China since 1900, *J. Meteorol. Res.*, 34, 243–251,  
646 <https://doi.org/10.1007/s13351-020-9839-6>, 2020.

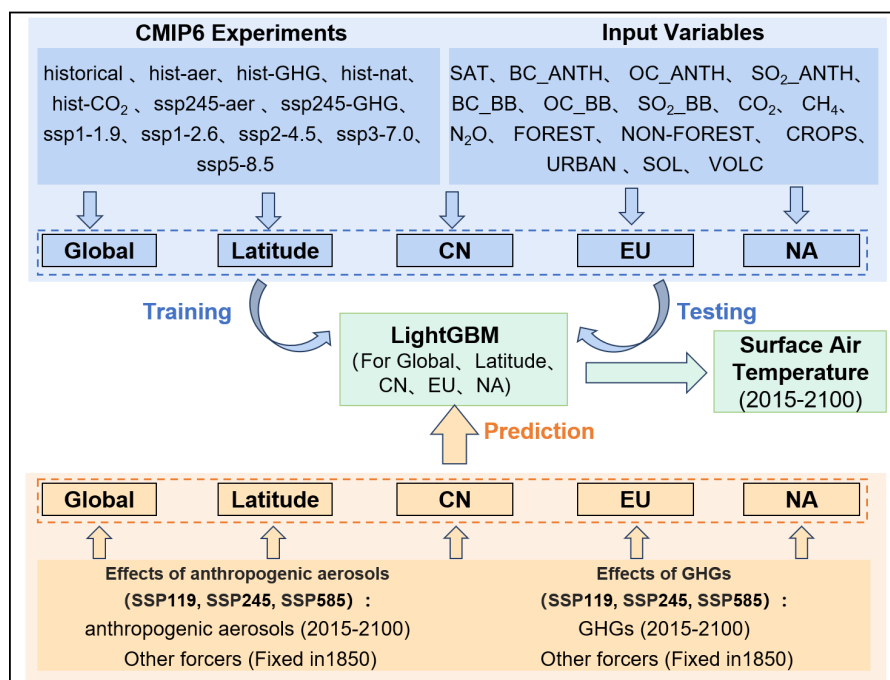


- 647 Yang, Y., Wang, H., Smith, S. J., Easter, R. C., and Rasch, P. J.: Sulfate aerosol in the  
648 Arctic: Source attribution and radiative forcing, *J. Geophys. Res. Atmos.*, 123,  
649 1899–1918, <https://doi.org/10.1002/2017JD027298>, 2018a.
- 650 Yang, Y., Wang, H., Smith, S. J., Zhang, R., Lou, S., Yu, H., Li, C., and Rasch, P. J.:  
651 Source apportionments of aerosols and their direct radiative forcing and long-term  
652 trends over continental United States, *Earth's Future*, 6, 793–808,  
653 <https://doi.org/10.1029/2018EF000859>, 2018b.
- 654 Yang, Y., Smith, S. J., Wang, H., Mills, C. M., and Rasch, P. J.: Variability, timescales,  
655 and nonlinearity in climate responses to black carbon emissions, *Atmos. Chem.*  
656 *Phys.*, 19, 2405–2420, <https://doi.org/10.5194/acp-19-2405-2019>, 2019.
- 657 Yang, Y., Lou, S., Wang, H., Wang, P., and Liao, H.: Trends and source apportionment  
658 of aerosols in Europe during 1980–2018, *Atmos. Chem. Phys.*, 20, 2579–2590,  
659 <https://doi.org/10.5194/acp-20-2579-2020>, 2020.
- 660 Yang, Y., Ren, L., Wu, M., Wang, H.\*, Song, F., Leung, L. R., Hao, X., Li, J., Chen, L.,  
661 Li, H., Zeng, L., Zhou, Y., Wang, P., Liao, H., Wang, J., and Zhou, Z.-Q.: Abrupt  
662 emissions reductions during COVID-19 contributed to record summer rainfall in  
663 China, *Nat. Commun.*, 13, 959, <https://doi.org/10.1038/s41467-022-28537-9>,  
664 2022.
- 665 Yang, Y., Zeng, L., Wang, H., Wang, P., and Liao, H.: Climate effects of future aerosol  
666 reductions for achieving carbon neutrality in China, *Sci. Bull.*, 68, 902–905,  
667 <https://doi.org/10.1016/j.scib.2023.03.048>, 2023.
- 668 Yu, H., Kaufman, Y. J., Chin, M., Feingold, G., Remer, L. A.: Anderson, T. L., Balkanski,  
669 Y., Bellouin, N., Boucher, O., Christopher, S., DeCola, P., Kahn, R., Koch, D.,  
670 Loeb, N., Reddy, M. S., Schulz, M., Takemura, T., and Zhou, M.: A review of  
671 measurement-based assessments of the aerosol direct radiative effect and forcing,  
672 *Atmos. Chem. Phys.*, 6, 613–666, <https://doi.org/10.5194/acp-6-613-2006>, 2006.



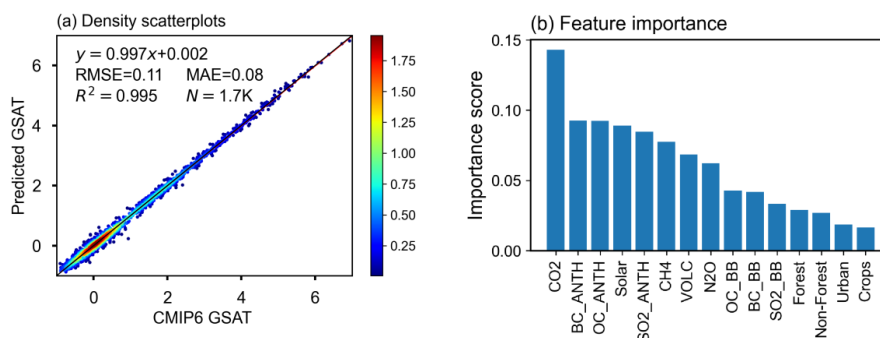
673 **Table 1.** Summary of datasets used in this study

| Dataset type                         | Variable              | Description                                                                                       | Spatial resolution | Temporal resolution | Time                                         | Source     |
|--------------------------------------|-----------------------|---------------------------------------------------------------------------------------------------|--------------------|---------------------|----------------------------------------------|------------|
| Meteorology                          | SAT                   | Surface air temperature                                                                           | 1°x1°              | Monthly             | 1850-2014 (historical)<br>2015–2100 (future) | CMIP6      |
| Emissions of aerosols and precursors | BC_ANTH               | Anthropogenic BC emissions                                                                        | 0.5°×0.5°          | Monthly             | 1850-2014 (historical)<br>2015–2100 (future) | input4MIPs |
|                                      | OC_ANTH               | Anthropogenic OC emissions                                                                        |                    |                     |                                              | input4MIPs |
|                                      | SO <sub>2</sub> _ANTH | Anthropogenic SO <sub>2</sub> Emissions                                                           |                    |                     |                                              | input4MIPs |
|                                      | BC_BB                 | Biomass burning BC emissions                                                                      |                    |                     |                                              | input4MIPs |
|                                      | OC_BB                 | Biomass burning OC emissions                                                                      |                    |                     |                                              | input4MIPs |
|                                      | SO <sub>2</sub> _BB   | Biomass burning SO <sub>2</sub> emissions                                                         | input4MIPs         |                     |                                              |            |
| GHGs concentrations                  | CO <sub>2</sub>       | Mole fraction of carbon dioxide in air                                                            | 0.5° for latitude  | Monthly             | 1850-2014 (historical)<br>2015–2100 (future) | input4MIPs |
|                                      | CH <sub>4</sub>       | Mole fraction of methane in air                                                                   |                    |                     |                                              | input4MIPs |
|                                      | N <sub>2</sub> O      | Mole fraction of nitrous oxide in air                                                             |                    |                     |                                              | input4MIPs |
| Land use                             | FOREST                | forested primary land and potentially forested secondary land                                     | 0.25°×0.25°        | Yearly              | 1850-2014 (historical)<br>2015–2100 (future) | input4MIPs |
|                                      | NON-FOREST            | non-forested primary land, potentially non-forested secondary land, managed pasture and rangeland |                    |                     |                                              |            |
|                                      | CROPS                 | C3 and C4 annual crops, C3 and C4 perennial crops and C3 nitrogen-fixing crops                    |                    |                     |                                              |            |
|                                      | URBAN                 | Urban land                                                                                        |                    |                     |                                              |            |
| Natural forcings                     | SOL                   | Solar irradiance                                                                                  | -                  | Monthly             | 1850-2100                                    | input4MIPs |
|                                      | VOLC                  | Layer volcanic aerosol mass mixing ratio                                                          | 5° for latitude    | Monthly             | 1850-2014 (historical)                       | input4MIPs |



675

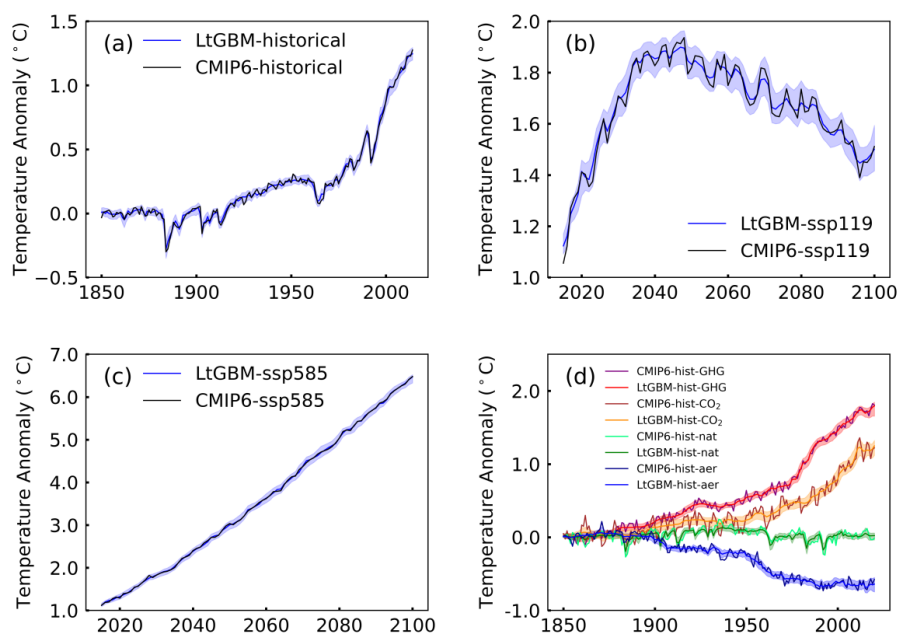
676 **Figure 1.** Flow diagram for predicting and attributing SAT under future climate  
 677 change using the LightGBM model. CMIP6 experiments and input variables are  
 678 described in Table S1 and Table 1, respectively.



679

680 **Figure 2.** (a) Scatterplot of the density of GSAT ( $^{\circ}\text{C}$ ) from CMIP6 multimodel mean  
681 versus the predicted values from the LightGBM model, with the color bars indicating  
682 the density of the data distribution. The black and red solid lines are the 1:1 line and  
683 the linear regression line, respectively. Statistical metrics including root mean square  
684 error (RMSE), mean absolute error (MAE), and coefficient of determination ( $R^2$ ) are  
685 given in the upper left corner of the panel (a). (b) Importance scores of input variables  
686 (aerosols, GHGs, land use, solar radiation and volcanic forcing) for the LightGBM  
687 model.

688



689

690 **Figure 3.** Time series of LightGBM-predicted GSAT anomalies ( $^{\circ}\text{C}$ ) and corresponding

691 CMIP6 values during (a) 1850–2014 and (b, c) 2015–2100 under the SSP1-1.9 and

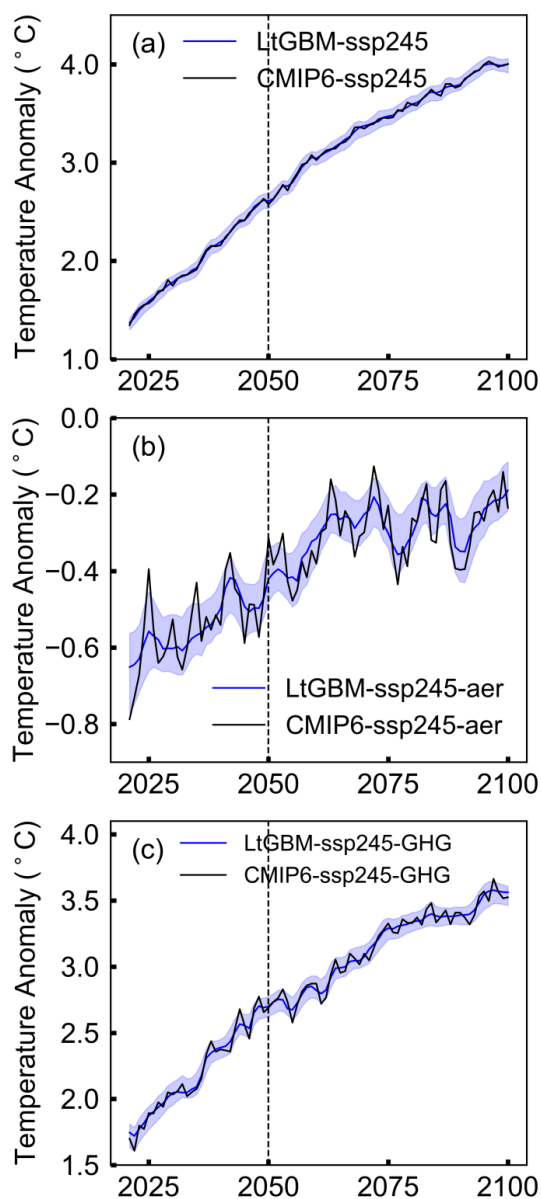
692 SSP5-8.5 scenarios. (d) Time series of GSAT anomalies attributed to historical changes

693 in GHGs,  $\text{CO}_2$ , natural forcings and anthropogenic aerosols predicted by LightGBM

694 and CMIP6 DAMIP during 1850–2020. Shaded areas indicate the range of the ML

695 prediction by random separation of training and testing datasets for 100 times.

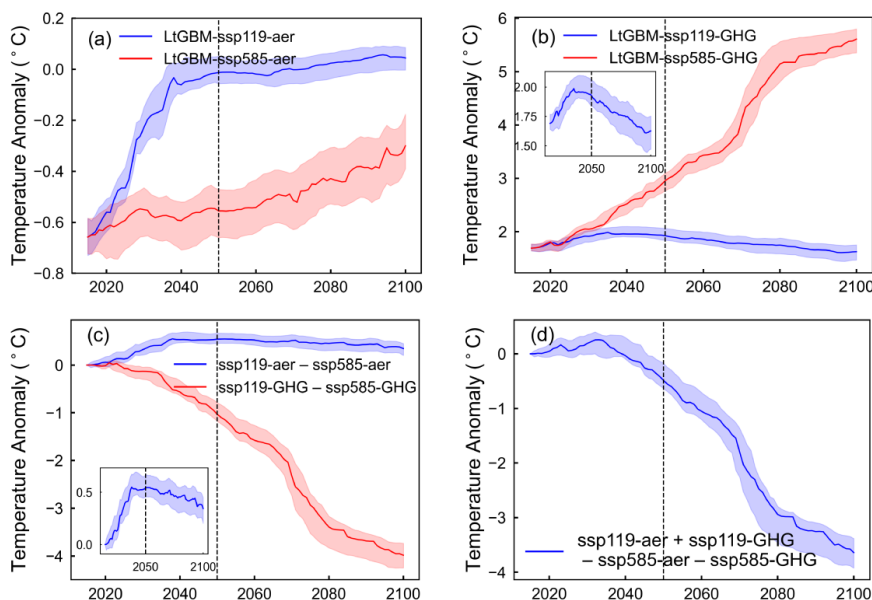
696



697

698 **Figure 4.** Time series of LightGBM-predicted GSAT anomalies (°C) and  
699 corresponding CMIP6 DAMIP values during 2021–2100 under the SSP2-4.5 scenario  
700 due to changes in (a) all forcing, (b) anthropogenic aerosols and (c) GHGs. Shaded  
701 areas indicate the range of the ML prediction by random separation of training and  
702 testing datasets for 100 times.

703



704

705 **Figure 5.** Time series of LightGBM-predicted GSAT anomalies (°C) during 2015–

706 2100 under the SSP1-1.9 and SSP5-8.5 due to changes in (a) anthropogenic aerosols

707 and (b) GHGs, and (c) changes in GSAT (°C) due to the future changes in

708 anthropogenic aerosols, GHGs, and (d) both of them in SSP1-1.9 relative to SSP5-8.5.

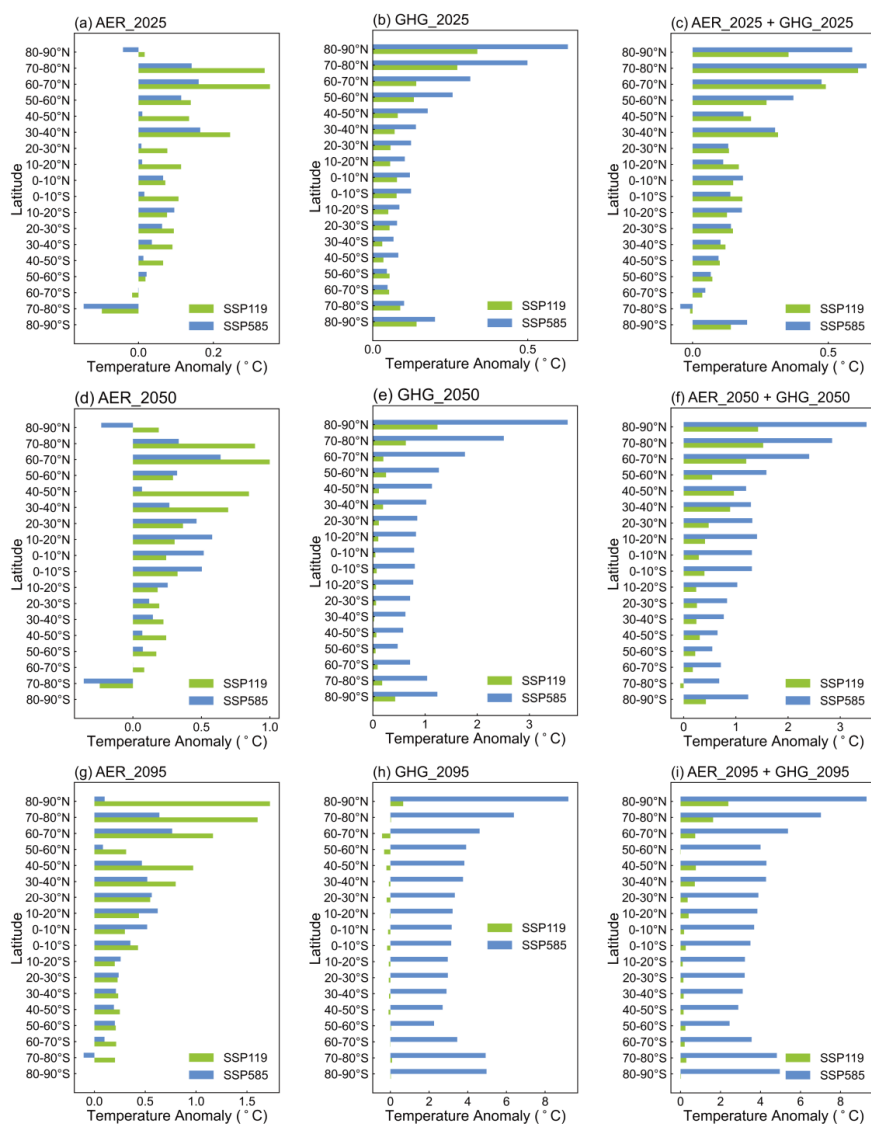
709 The inner figure in (b) is the GSAT anomalies due to changes in GHGs under the SSP1-

710 1.9 scenario. The inner figure in (c) is GSAT anomalies induced by anthropogenic

711 aerosols in SSP1-1.9 relative to SSP5-8.5. Shaded areas indicate the range of the ML

712 prediction by random separation of training and testing datasets for 100 times.

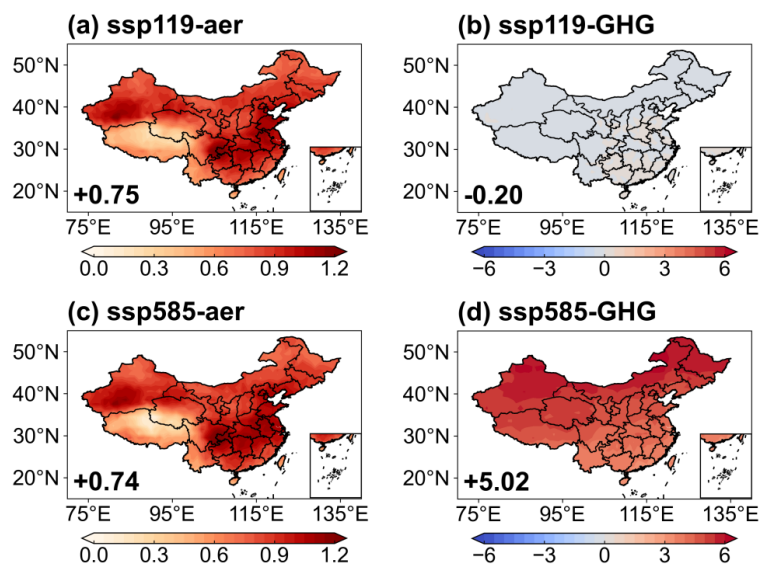
713



714

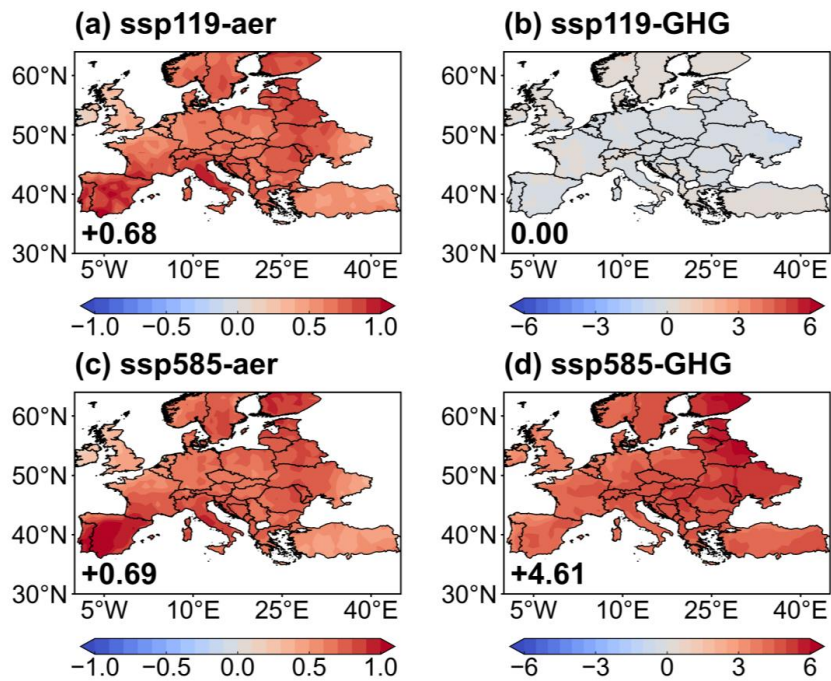
715 **Figure 6.** Attribution of changes in SAT (°C) in each 10° latitudinal band from 90°S to  
 716 90°N to future changes in anthropogenic aerosols (left), GHGs (middle) and both of  
 717 them (right) in 2025 (averaged 2021–2030), 2050 (averaged 2045–2054) and 2095  
 718 (averaged 2091–2100) (from top to bottom) relative to 2020 (averaged over 2015–2024)  
 719 under the SSP1-1.9 and SSP5-8.5 scenarios, as predicted by the LightGBM models.

720



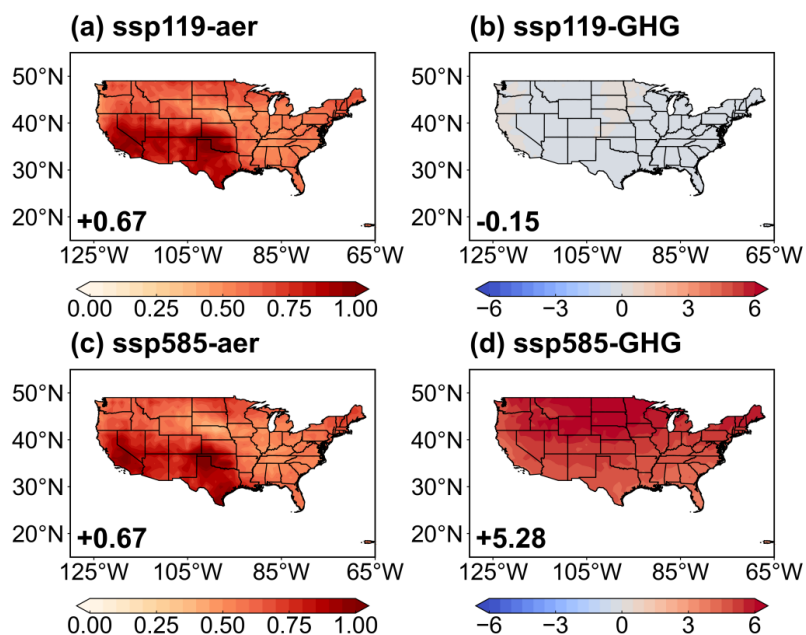
721

722 **Figure 7.** Attribution of changes in SAT (°C) in China to future changes in  
723 anthropogenic (a, c) aerosols and (b, d) GHGs in 2095 (averaged 2091–2100) relative  
724 to 2020 (averaged over 2015–2024) under the SSP1-1.9 and SSP5-8.5 predicted by  
725 the LightGBM models. The regional averages are shown in bottom left of each panel.  
726 Note that the color bars have different ranges between aerosols and GHGs change.



727

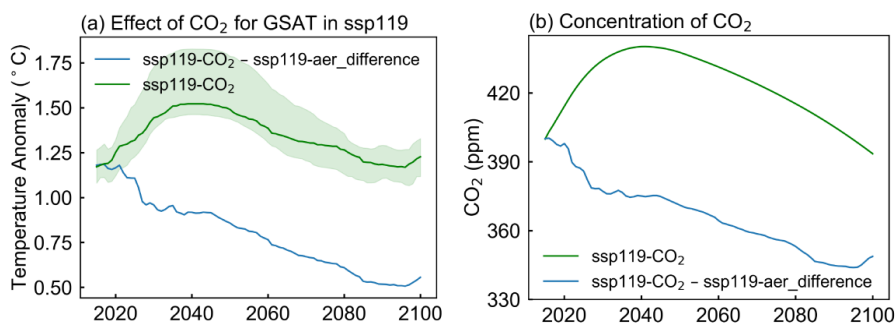
728 **Figure 8.** Same as Fig.7, but for Europe.



729

730 **Figure 9.** Same as Fig.7, but for North America.

731



732

733 **Figure 10.** (a) Time series of LightGBM-predicted GSAT anomalies (°C) during 2015–  
734 2100 under the SSP1-1.9 due to changes in CO<sub>2</sub> (green line) and the additional cooling  
735 to offsetting the warming induced by aerosol reduction (blue line). (b) Global CO<sub>2</sub>  
736 concentrations from the SSP1-1.9 (green line) and required concentrations for meeting  
737 the GSAT anomalies in (a) (blue line). The required concentrations are from the look-  
738 up table created by the LightGBM model through linearly perturbing CO<sub>2</sub>  
739 concentrations.